CO₂

CO

Solid Oxide Electrolysis Cell

O₂

**Showcasing research from Dr Tae Ho Shin's laboratory, Hydrogen Energy Material Centre, Korea Institute of Ceramic Engineering and Technology, Republic of Korea.**

Enhancing $CO_2$ electrolysis performance with various metal additives (Co, Fe, Ni, and Ru) – decorating the La(Sr)Fe(Mn)$O_3$ cathode in solid oxide electrolysis cells

A promising metal-infiltrated ceramic electrode for high-temperature $CO_2$ electrolysis cells with a LaGaO₃-based solid oxide electrolyte is reported, suggesting accelerated chemical adsorption of $CO_2$ *via* metal additives on the ceramic electrode and presenting an insight into the surface activity of metal catalysts in $CO_2$ electrolysis.
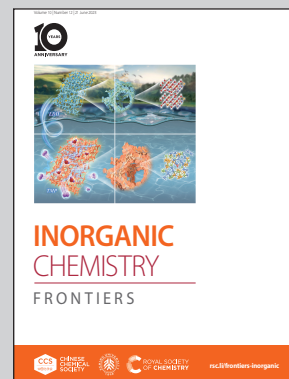
Registered charity number: 207890

CCS 中国化学会 CHINESE CHEMICAL SOCIETY

PEKING UNIVERSITY 1898

ROYAL SOCIETY OF CHEMISTRY

**rsc.li/frontiers-inorganic**

## RESEARCH ARTICLE

Check for updates

# Enhancing CO₂ electrolysis performance with various metal additives (Co, Fe, Ni, and Ru) – decorating the La(Sr)Fe(Mn)O₃ cathode in solid oxide electrolysis cells†

Sang Won Lee,‡[a,b] Tae Heon Nam,‡[a,c] Minkyu Kim,[a] Seokhee Lee,[a] Kyu Hyung Lee, [ID] *[c] Jong Hyeok Park [ID] *[b] and Tae Ho Shin [ID] *[a]

Perovskite oxide shows great promise as an alternative fuel electrode material in solid oxide electrolysis cells (SOEC) for the specific CO₂ electrochemical reduction, because of its excellent coking resistance. However, use of perovskite oxide is limited by its poor catalytic activity in CO₂ reduction. In this study, we investigated the use of various metal additives (Co, Fe, Ni, and Ru) on a La(Sr)Fe(Mn)O₃ (LSFM) fuel electrode for CO₂ reduction in a commercial infiltration process. Based on the electrochemical impedance spectroscopy (EIS) results, we determined the catalytic activity and reaction kinetics of CO₂ reduction for metal catalysts. In addition, the distribution of relaxation times analysis was conducted to investigate the adsorption and dissociation processes of CO₂ molecules for each catalyst. Consequently, when the Fe catalyst was applied in a LSFM fuel electrode for $La_{0.8}Sr_{0.2}Ga_{0.8}Mn_{0.2}O_3$ (LSGM) electrolyte-supported cells, an electrolysis performance of 2.201 A cm⁻² at 1.5 V in CO₂ electrolysis was obtained at 1123 K.

## Introduction

With the rapidly increasing energy demand worldwide, fossil fuel consumption, which accounts for 85% of the supplied energy, has caused energy and climate crises because of the associated CO₂ emissions. Due to sustainability challenges, global energy and emission policies aim for net-zero or net-negative emissions of greenhouse gases, including CO₂, by the year 2050.[1–3] Therefore, researchers are currently focused on electrochemical CO₂ reductions of fuel and chemical feedstocks to create a sustainable society.[4–7] However, the C=O bond energy in CO₂ shows an intrinsic stability of 806 kJ mol⁻¹, which makes CO₂ reduction challenging, especially at low temperatures.[8–11] Moreover, solid oxide electrolysis cells (SOECs) show great potential as promising electrochemical devices for carbon capture and utilization, because they enable highly efficient direct conversion of CO₂ to CO. The operating

temperature of the SOEC (>1073 K) can accelerate the processes involved in CO₂ reduction, such as molecular adsorption and dissociation. In addition, CO, a product of CO₂ reduction, has been widely used in industrial applications, where it is smelted to metal by using reducing oxides or is converted to syngas by the Fischer–Tropsch process.[12,13]

The electrochemical reactions in SOECs are mostly dominated by the fuel electrode, where the CO₂ reduction is performed at the electrode surface. The Ni-based fuel electrodes are commonly used in SOECs because of their high electrochemical activity and good conductivity for current collection. However, Ni electrodes suffer from inhibition of the redox instability, or deactivation of Ni due to a carbon buildup (coking) on the Ni electrode surface when directly exposed to a CO₂/CO atmosphere.[14–16] Therefore, from the perspective of CO₂ electrolysis in SOECs, alternative materials with catalytic activity, electrical conductivity (EC), and durability in the CO/CO₂ redox reaction are essential. Consequently, perovskite oxide is attracting attention as a candidate because of its excellent CO₂ redox stability and carbon coking tolerance.[15,17,18] Among these, the La(Sr)FeO₃-based perovskite oxides have high ionic and electrical conductivities, as well as catalytic properties because of the Fe⁴⁺/Fe³⁺ couple, which is compensated for by oxygen vacancies.[19] The abundant oxygen vacancies in Fe-based perovskite oxides can provide active sites for CO₂ adsorption and dissociation.[20,21] For example, Ishihara *et al.* have reported that Mn-doped $La_{0.6}Sr_{0.4}Fe_{1-x}Mn_xO_3$ used as a

[a]*Korea Institute of Ceramic Engineering and Technology, Jinju-si, Gyeongsangnam-do 52851, Republic of Korea. E-mail: ths@kicet.re.kr*
[b]*Department of Chemical and Biomolecular Engineering, Yonsei University, 50 Yonsei-ro, Seodaemun-gu, Seoul 120-749, Republic of Korea. E-mail: lutts@yonsei.ac.kr*
[c]*Department of Materials Science & Engineering, Yonsei University, 50 Yonsei-ro, Seodaemun-gu, Seoul 120-749, Republic of Korea. E-mail: khlee2018@yonsei.ac.kr*
†Electronic supplementary information (ESI) available: Supplementary figures. See DOI: https://doi.org/10.1039/d3qi00379e
‡These authors contributed equally.

**3536** | *Inorg. Chem. Front.*, 2023, **10**, 3536–3543

This journal is © the Partner Organisations 2023

fuel electrode showed high activity for $CO_2$ electrolysis without coke deposition under $CO_2$ (50%)–CO-Ar (1%) conditions, at a relatively low oxygen partial pressure.[22] Furthermore, Peng *et al.* reported an excellent phase stability and carbon tolerance of the $La_{0.6}Sr_{0.4}Fe_{0.9}Mn_{0.1}O_3$ (LSFM) fuel electrode for $CO_2$ electrolysis in a symmetrical cell. However, these cell performances are still insufficient because of their lower EC and catalytic activity compared to conventional Ni-based fuel electrodes.[22,23] To solve this problem and achieve a higher performance, an additional catalyst was blended into the fuel electrode. Ishihara and co-workers also reported Ni–Fe mixed with La(Sr)Fe(Mn)$O_3$ as a composite metal/ceramic fuel electrode, which displayed a remarkable performance by increasing the catalytic activity and number of reaction sites for $CO_2$ reduction.[24] Therefore, because the addition of suitable catalysts to promote $CO_2$ reduction plays an important role, research should be conducted on various metal catalysts in SOECs.

Herein, we report on the investigation of the use of various metal catalysts (Co, Fe Ni, and Ru) as active additives on the surface of LSFM using the infiltration method. These metal additives affect the surface-absorption energies of the metal catalysts, which accelerate the chemical adsorption of $CO_2$. The metal catalysts were validated using electrochemical impedance spectroscopy (EIS), and their electrochemical properties. Moreover, the performance of the metal-added LSFM electrode was characterized using $La_{0.8}Sr_{0.2}Ga_{0.8}Mg_{0.2}O_3$ (LSGM) electrolyte-supported cells, and these metal catalysts improved the electrocatalytic activity of the fuel electrode for $CO_2$ reduction in SOECs.

## Experimental section

### The SOEC preparation

An LSGM electrolyte-supported cell was used to measure its high electrochemical ability. A disk of the electrolyte was prepared by uniaxial pressing, using commercially available LSGM powders (Fuel Cell Materials, USA) at 30 MPa, followed by sintering at 1773 K for 5 h to obtain a high densification of the electrolyte. The thickness of the LSGM electrolyte was adjusted to 200 μm by polishing. The LSFM and the $Sm_{0.5}Sr_{0.5}CoO_3$ (SSC, Kceracell, Korea) electrode materials were mixed with a terpineol-based ink vehicle (Fuel Cell Materials, USA) in a three-roll mill to produce uniformly mixed pastes. Both pastes were screen-printed on each side of the electrolyte with a working area of 0.196 $cm^2$, and they were co-sintered at 1273 K for 1 h.

### Metal infiltration process

For metal infiltration, $Ru(NO)(NO_3)_3$ (Alfar Aesar, USA), $Co(NO_3)_2 \cdot 6H_2O$ (Sigma-Aldrich, USA), $Fe(NO_3)_3 \cdot 9H_2O$ (Wako Chemicals, Japan), and $Ni(NO_3)_2 \cdot 6H_2O$ (Alfar Aesar, USA) were employed as metal precursors. A stoichiometric concentration of 0.001 M of the infiltration precursor was fully dissolved in distilled water. Acetone was then added to the solution to reduce the surface tension. Subsequently, 5 μL of the metal precursor solution was lightly dropped onto the LSFM electrode using a micropipette. The metal-precursor-infiltrated samples were then completely dried at room temperature. The dried samples were fired at 673 K for 30 min to decompose the organic compounds. Subsequently, the samples were sintered for crystallization at 1073 K for 1 h.

### Characterization

X-ray diffraction (XRD) analysis (D8 DISCOVER, Bruker, Germany) was performed to determine the crystal structure of the electrode, and to confirm the chemical compatibility between the infiltrated metal catalyst and the electrode. This was investigated in the $2\theta$ range of 10–90° with Cu Kα radiation ($\lambda = 1.5406$ Å). The morphology and microstructure of the infiltrated metal particles on the LSFM electrode were confirmed using field-emission scanning electron microscopy (FE-SEM, JSM-7610F, Jeol, Japan). The $CO_2$ temperature-programmed desorption (TPD) was measured to clarify the physiochemical characterization of the $CO_2$ reduction in the electrode. After the adsorption process in 10% $CO_2$–He at 773 K for 1 h, the analysis was performed up to 1173 K under He.

### Electrochemical performance of the LSGM-based cell

To test the performance of the fabricated cell, a gold-grid (Heraeus, USA), for current collection, was screen-printed onto both the fuel and air electrodes. The cells were measured using two alumina pipes attached to a Pyrex glass ring for gas-sealing. Each electrode was in contact with a Pt mesh and lead lines for electrochemical evaluation. For fuel cell performance, 3% humidified hydrogen and oxygen were supplied to the chamber as the fuel and oxidant, respectively. In addition, a $CO_2$ : CO gas mixture (50 : 50) was fed as the fuel for $CO_2$ electrolysis. This gas feeding was controlled to 100 mL min$^{-1}$ by a mass flow controller. To evaluate the electrochemical properties of the LSFM electrode, the current–voltage characteristics ($I$–$V$) were measured using a potentiostat (VMP-300, BioLogic, France). Impedance measurements were performed using the potentiostat with an AC amplitude of 30 mV. The frequency of the impedance ranged from 0.1 Hz to 1 MHz. Furthermore, the EIS data were fitted using ZView software, which could implement an equivalent circuit model. The internal resistance overpotentials of the metal-infiltrated cells were measured using the current interruption method. To better characterize the performance of the electrode impedance process, the distribution of the relaxation time was analyzed (MATLAB) using the complex nonlinear least-squares method. The regularization parameter was $10^{-4}$. The faradaic efficiency (FE) was calculated by using gas chromatography (6890N, Agilent, USA) with a Carboxen 1000 columns.

## Results and discussion

The infiltration process causes various catalytic activities at existing porous electrodes. A wet process involving metal salt

This journal is © the Partner Organisations 2023

*Inorg. Chem. Front.*, 2023, **10**, 3536–3543 | **3537**

precursors was introduced into the porous LSFM electrode. After subsequent heat treatment, the metal catalysts formed on the surface of the LSFM electrode. The XRD analysis was performed to confirm the chemical stability and formation of the metal catalysts on the LSFM electrode after the infiltration process. Fig. 1 shows the XRD patterns of bare and metal-infiltrated LSFM after heat treatment at 1073 K for 1 h. The LSFM materials only showed a pattern corresponding to perovskite-based $LaFeO_3$ (JCPDS 37-1493), which has an orthorhombic structure as the dominant phase. After the infiltration process, the patterns confirmed the crystallinity of the perovskite phase without distinct impurity peaks of the secondary phases,
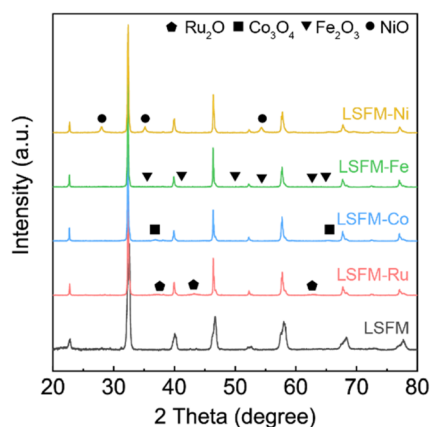
which indicated the stability of the metal catalyst on the LSFM backbone. In addition, the metal-based catalysts were identified by their intrinsic peaks in the form of metal oxides. These metal catalysts were expected to improve cell performance by accelerating the adsorption and dissociation of the $CO_2$ molecules during the $CO_2$ electrolysis.[25,26]

Fig. 2 shows the HR-SEM images which demonstrate the microstructure of the LSFM and the infiltrated LSFM electrodes. The images show that each metal particle is visible on the internal LSFM surface, leading to an increase in surface roughness. In addition, the EDS mapping indicates a high degree of overlap in the distribution of Co, Fe, Ni, and Ru, which is consistent with the LSFM backbone. These observations confirmed that the metal nanocatalyst is evenly dispersed across the LSFM surface. Although there are slight differences in particle size, the metal particles have high coverage and are well-distributed at the nanoscale, which can also be expected to have a nano size effect. These well-distributed nanoparticles are ideal for extending the reactive active sites to enhance the electrode reactions. In the electrochemical reactions, metal catalysts adsorb $CO_2$ molecules to form carbonate intermediates, which rapidly provide electrons to accelerate the dissociation reaction into CO and $O^{2-}$. In addition, the well-distributed nanoparticles are ideal for enhancing the electrode reaction by expanding the reactive active sites and triple-phase boundaries (TPBs).[27] Therefore, in addition to $CO_2$ electrolysis, the metal-infiltrated LSFM is superior to LSFM in humidified hydrogen fuel cells.

Fig. 3a shows the *I–V* curves of the cell containing the LSFM and infiltrated LSFM electrodes under humidified hydrogen at 1073 K. Overall, the addition of metal catalysts improved the
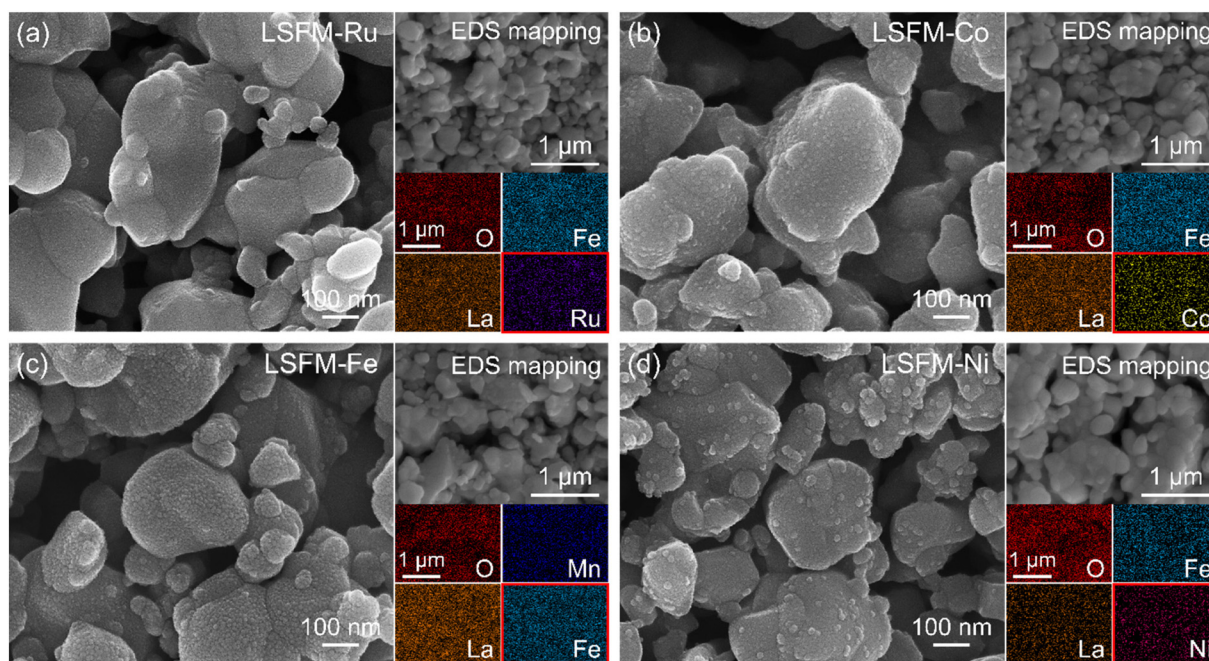


**Fig. 1** X-ray diffraction (XRD) patterns of bare and infiltrated LSFM electrodes with various metal-based catalysts (Co, Fe, Ni, and Ru) after sintering at 1073 K.



**Fig. 2** Scanning electron microscopy (SEM) images and EDS mapping results taken for (a) LSFM-Ru, (b) LSFM-Co, (c) LSFM-Fe, and (d) LSFM-Ni electrodes after sintering at 1073 K.
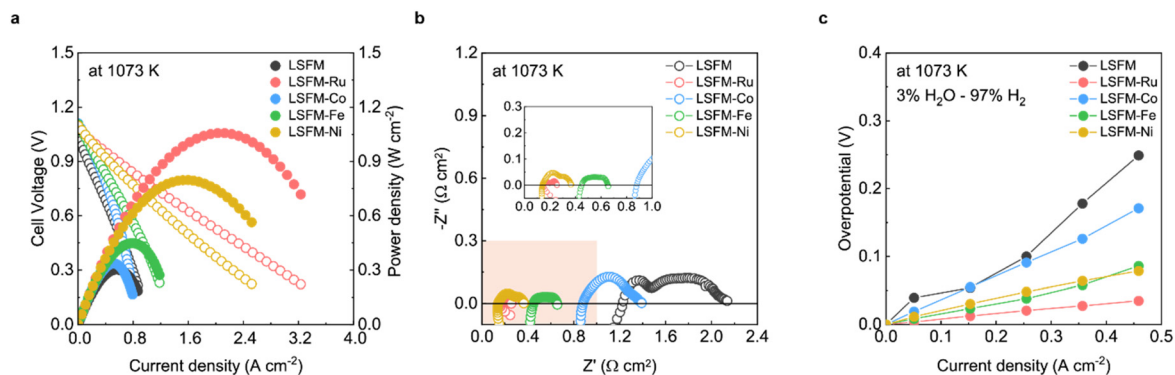
**3538** | *Inorg. Chem. Front.*, 2023, **10**, 3536–3543

This journal is © the Partner Organisations 2023

**Fig. 3** (a) The I-V curves and (b) the impedance data of single cells of LSFM and infiltrated LSFM electrodes (Co, Fe, Ni, and Ru) at 1073 K under $H_2O : H_2$ (3%:97%). (c) The polarization overpotential is calculated from the impedance data.

performance of the cell. The LSFM-Ru electrode cell achieved the highest performance of approximately 1.05 W cm$^2$ which is about twice the maximum power density of a bare LSFM cell (0.56 W cm$^2$). As shown in Fig. 3b, the ohmic resistance ($R_o$) was calculated from the intercept point of the high-frequency region along the real axis of the Nyquist-plots. After infiltration, the $R_o$ decreases, which is likely to be because the metal precursor solution improves the interfacial stability between each particle and layer.[28] In terms of the polarization resistance, which accounts for the electrochemical reactions, the overpotential was estimated by using the current interruption method (Fig. 3c) as a function of current density. As expected, the electrochemical reaction of the bare LSFM was enhanced because of metal catalytic activity. For the LSFM-Ru, the overpotential was significantly decreased compared to that of the others at under humidified hydrogen (Ru > Fe ≥ Ni > Co). This result implies that the various metal catalysts decrease the molecular surface activation energy of the electrode, enhancing the electrochemical reaction of SOFC under a hydrogen atmosphere.

To evaluate the electrochemical performance of the $CO_2$ reduction for electrolysis, the cell containing the LSFM and the infiltrated LSFM electrodes was tested under a blend of $CO_2 : CO$ gases (50 : 50) at 1123 K, the results of which are shown in Fig. 4. Table 1 summarizes the open-circuit voltage (OCV), cell performance, and resistance values obtained from the EIS data with the different metal catalysts. In the $CO_2 : CO$ (50 : 50) atmosphere, the OCV of the LSFM-based electrodes was approximately 0.96 V, which is close to the theoretical value expected from the Nernst equation, and this indicated the good gas-sealing of the cell.[29] Moreover, the satisfactory

**Table 1** The electrochemical properties of $CO_2$ electrolysis with LSFM and metal-infiltrated LSFM at 1123 K: open-circuit voltage (OCV), the current density at 1.5 V, and the EIS results

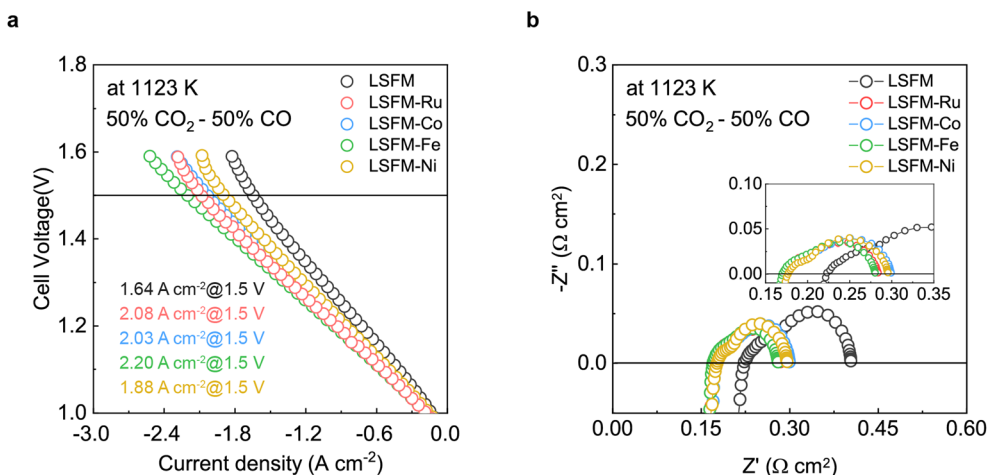| Sample | OCV | Current density @1.5 V (A cm$^{-2}$) | $R_o$ (Ω cm$^2$) | $R_p$ (Ω cm$^2$) |
|---|---|---|---|---|
| LSFM | 0.961 | 1.640 | 0.223 | 0.182 |
| LSFM-Ru | 0.961 | 2.084 | 0.172 | 0.112 |
| LSFM-Co | 0.962 | 2.034 | 0.176 | 0.123 |
| LSFM-Fe | 0.963 | 2.201 | 0.171 | 0.110 |
| LSFM-Ni | 0.963 | 1.879 | 0.177 | 0.119 |



**Fig. 4** (a) The $CO_2$ electrolysis performance with the infiltrated LSFM electrode feeding $CO_2 : CO$ (50 : 50) at 1123 K. (b) Total impedance spectra of the cell with the infiltrated LSFM electrode at 1123 K.

This journal is © the Partner Organisations 2023

*Inorg. Chem. Front.*, 2023, **10**, 3536–3543 | **3539**

linear relationships between current density and voltage imply that the fuel $CO_2/CO$ mixture is an appropriate feedstock without cell starvation at a high current density.

From the $I$–$V$ curve shown in Fig. 4a, it can be seen that the LSFM-Fe electrode achieved a current density of 2.201 A cm$^{-2}$ when 1.5 V was applied. This value is higher than those of the other cells (1.640, 2.084, 2.034, and 1.879 A cm$^{-2}$ for the different electrodes of LSFM, LSFM-Ru, LSFM-Co, and LSFM-Ni, respectively). Therefore, the Fe infiltration of the LSFM electrode has good catalytic activity in the $CO_2$ reduction reaction of a SOEC (Fe > Ru ≥ Co > Ni). According to the EIS results shown in Fig. 4b, $R_o$ and $R_p$ were decreased by the infiltration process, which is consistent with the results shown in Fig. 3. In terms of $R_p$ interpreted as electrochemical reactions, the LSFM-Fe electrode showed a lower $R_p$ value of 0.110 Ω cm$^2$ among the infiltration applications. Contrary to the fuel cell mode, the Fe metal additives had a better catalytic activity than others in the $CO_2$ electrolysis mode. However, the Ru additives also showed a fairly good performance as an additive to enhance the surface catalytic activity for the $CO_2$ reduction. This observation can be attributed to the varying electrochemical $CO_2$ reduction by the metal catalyst, which depends on the extent of chemisorption of the $CO/CO_2$ molecules on the different metal surfaces.

To further identify the effect of the metal catalyst on the LSFM electrode, we calculated the activation overpotential, which is expressed as:[30]

$$\eta_{act} = E_{OCV} - V_{measure} - \eta_{ohmic} = E_{OCV} - V_{measure} - iR_{ohmic}$$

where $E_{OCV}$ denotes the OCV value, $V_{measure}$ denotes the voltage applied at a specific current density (i) in the $I$–$V$ curves, $i$ denotes the current density, and $R_{ohmic}$ denotes the ohmic resistance of the electrolyte from the EIS results. When $\eta_{act}$ is large, the Butler–Volmer equation can be simplified to estimate the activation overpotential:

$$\eta_{act} = -\frac{RT}{\alpha nF}\ln(i_0) + \frac{RT}{\alpha nF}\ln(i)$$

where $R$ denotes the gas constant, $T$ denotes the temperature, $F$ denotes the Faraday constant (96 485 C mol$^{-1}$), $n$ represents the number of electrons for $CO_2$ electrolysis ($n$ = 2), and $i_0$ and $\alpha$ are the exchange current density and the charge transfer coefficient, respectively, which were determined using Tafel fitting at 0.1–0.2 V. Fig. 5 and Table 2 show the $i_0$ and $\alpha$ values of the LSFM-based cells. For $CO_2$ reduction in the electrolytic mode, the α values of the LSFM-based electrode cells were less than 0.5. This might be explained by the relatively lower conductivity of the LSGM electrolytes than that of the liquid system, plus the solid electrolyte strongly depends on temperature, and thus they behave like non-liquid electrolytes.[31] In the case of the LSFM-based electrode cells on the LSGM electrolyte, the LSFM, LSFM-Ru, LSFM-Co, LSFM-Fe, and LSFM-Ni had α values of 0.31, 0.31, 0.32, 0.34, and 0.30, respectively. However, these results do not present a major problem because the introduction of a catalyst enhances the electrochemical reaction. For the calculated exchange current density, the LSFM-Fe and LSFM-Ru electrodes exhibited a superior $i_0$ (0.664 A cm$^{-2}$ and 0.651 A cm$^{-2}$, respectively) to that of the bare LSFM electrode (0.548 A cm$^{-2}$). The value of $i_0$ was increased by introducing a metal catalyst, which is consistent with the cell performance discussed previously (Fe > Ru ≥ Co > Ni). An increase in $i_0$ suggested that metal catalysts, especially Fe and Ru, accelerated the electrode surface exchange kinetics.[32] Because SSC was equally applied to the

**Table 2** Exchange current density ($i_o$) and the transfer coefficients ($\alpha$) of LSFM, LSFM-Co, LSFM-Fe, LSFM-Ni, and LSFM-Ru electrodes

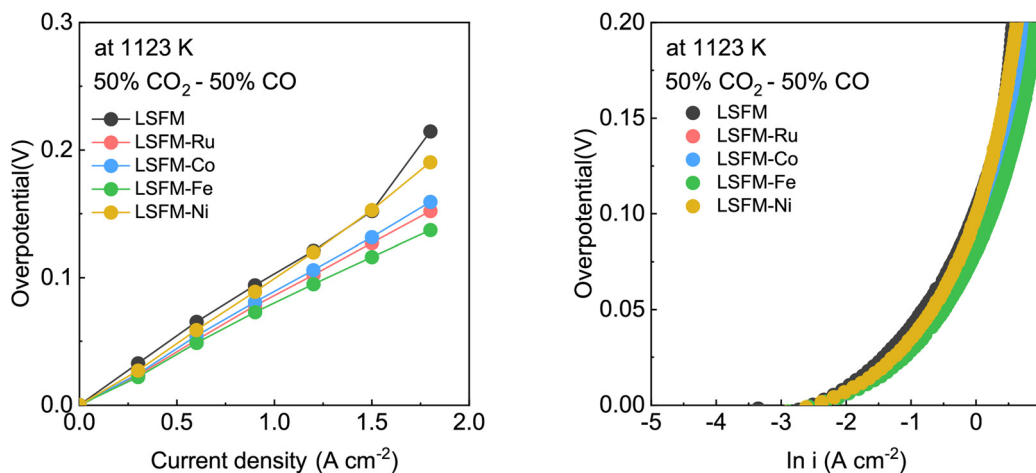| Sample | $\alpha$ | $i_o$(A cm$^{-2}$) |
|---|---|---|
| LSFM | 0.31 | 0.548 |
| LSFM-Ru | 0.31 | 0.651 |
| LSFM-Co | 0.32 | 0.622 |
| LSFM-Fe | 0.34 | 0.664 |
| LSFM-Ni | 0.30 | 0.573 |



**Fig. 5** (a and b) The Tafel plot (fitted with an overpotential of 0.1–0.2 V) of the LSFM and metal-infiltrated LSFM electrodes (Co, Fe, Ni, and Ru) in the $CO_2$ electrolysis at 1123 K.

**3540** | *Inorg. Chem. Front.*, 2023, **10**, 3536–3543

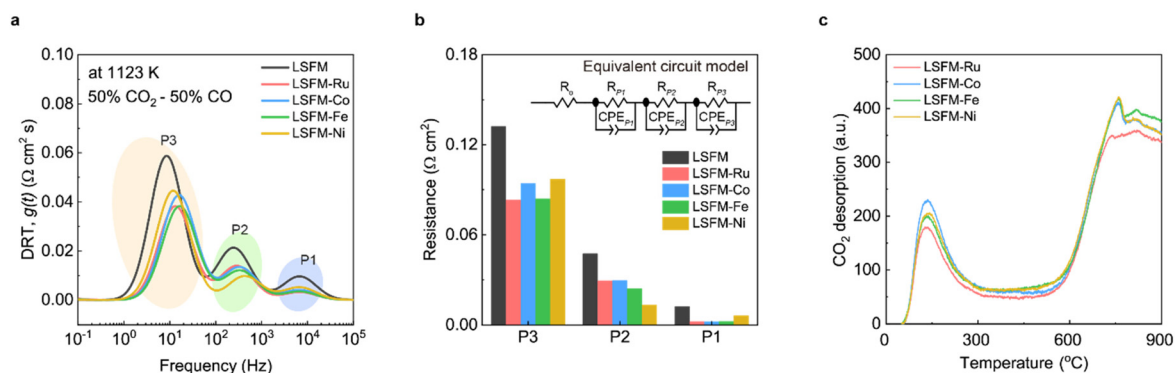This journal is © the Partner Organisations 2023

**Fig. 6** (a) Comparison of plots of the distribution of relaxation times (DRT) for LSFM and the infiltrated LSFM electrodes at 1123 K. (b) Polarization resistance of each cell calculated from the circuit model fitting results, and (c) the $CO_2$-TPD profiles of the metal infiltrated LSFM.

oxygen electrodes of all the cells, the improvement of $\alpha$ and $i_0$ can mainly contribute to the metal-infiltrated fuel electrode.

To gain a deeper insight into the kinetics of the electrochemical reactions in metal-incorporated electrodes, the distribution of the relaxation time analysis was performed using the EIS data.[33] Fig. 6a shows the plots of the distribution of the relaxation time for the electrochemical processes for the electrodes at 1123 K in $CO_2$ electrolysis. The electrochemical process can be deconvoluted into three peaks (P1, P2, and P3), as shown in Fig. 6a. Specific peaks represent the rate-determining steps (RDSs) of the electrochemical reactions. P1 is concerned with the transfer of $O^{2-}$ through the interface between the electrode and the LSGM electrolyte. P2 is correlated with the dissociation of the adsorbed $CO_2$ molecules into carbonate intermediates and CO. P3 is associated with the adsorption of $CO_2$ molecules onto the electrode surface.[34] For the LSFM electrode, the reactions in all the processes were enhanced by introducing a metal catalyst. To quantify the contribution of each process from the impedance results, an equivalent circuit model was used based on the distribution of the relaxation time analysis at 1123 K (Fig. 6b). The value of $R_{P1}$ decreased

because of the improved interfacial stability between the electrode and electrolyte during infiltration. The value of $R_{P1}$ of the LSFM-Ni electrode cell was higher than that of the other metal-infiltrated electrode cells. This was probably due to the slight reactivity with the electrolyte, which is consistent with the $R_0$ results of the impedance.[35] In the P2 process, the metal nanoparticle was strongly concerned with the dissociation process of the adsorbed $CO_2$ molecules by the donating electrons.[36] In our case, the Ni catalyst showed the best catalytic activity in the P2 process, followed by Ni > Fe > Ru ≥ Co. This may be attributed to the interaction between the metal particles and the carbonate intermediate on the LSFM electrode. Consequently, various factors caused by the catalytic activity of the metal particles, and the interaction between metal catalysts and perovskite oxides, should be considered when selecting the optimal catalyst. Because this is unclear, further studies on the use of SOECs are still required. For $CO_2$ electrolysis at the fuel electrode, $CO_2$ adsorption, which is the initial step in the electrochemical $CO_2$ reduction, is also important. In the subsequent P3 process, the Fe and Ru catalysts showed smaller peaks compared to the Co and Ni catalysts, suggesting that
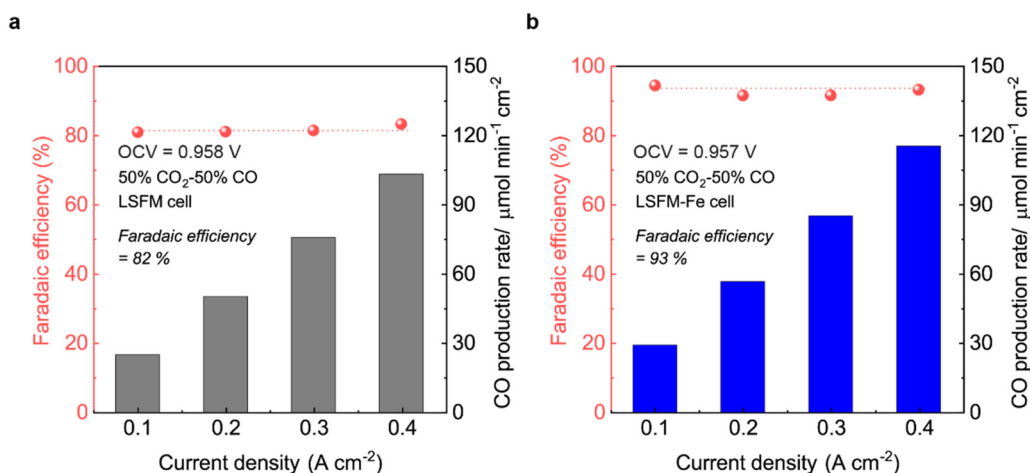


**Fig. 7** Faradaic efficiency of the cell with (a) bare LSFM, and (b) LSFM-Fe electrode with a $CO_2$ : CO gas (50 : 50) mixture at 1123 K.

This journal is © the Partner Organisations 2023

*Inorg. Chem. Front.*, 2023, **10**, 3536–3543 | **3541**

they had a stronger or more favorable impact on the adsorption behavior of $CO_2$. These comprehensive results suggest that appropriate metal catalysts should be explored from various perspectives, such as molecular adsorption and dissociation. In order to investigate the adsorption and desorption process in the metal-infiltrated electrodes for $CO_2$ reduction, $CO_2$-TPD was conducted as shown in Fig. 6c. The results obtained revealed the presence of two distinctive peaks at 373–573 K and 873–1173 K for all the electrodes. Interestingly, the Fe catalyst exhibited the strongest peak in the high-temperature range, which corresponds to the operating temperature of the SOECs. This finding indicates the superior performance of Fe catalyst at high temperatures, as it activates more active sites for $CO_2$ adsorption and dissociation.

Fig. 7 illustrates the FE of the LSFM and LSFM-Fe electrode cells under varying current densities. The FE can be calculated by the following equation by using the measured CO production rates in the composition of the gas outlets:

$$FE = \frac{n_{CO,measured}}{I \times n \times F} \times 100 \; (\%),$$

where $I$ is the current density and $n_{CO,measured}$ is the measured CO production rates in the EC mode. The $n_{CO,measured}$ gradually increased as higher electrolysis currents were applied. The LSFM-Fe electrode exhibited a high FE at about 93%, which is attributed to the high surface activity of the metal catalyst, compared to the LSFM electrode with an FE of 83%. These results suggested that the Fe nanoparticles in the LSFM electrode have a good $CO_2$ reduction activity, making the LSFM-Fe electrode more efficient for $CO_2$ conversion.

## Conclusions

In this study, we investigated the activity of various metal catalysts on LSFM fuel electrodes for the electrochemical oxidation of $H_2$, and $CO_2$ reduction. The Ru catalyst on the LSFM electrode had the best electrochemical performance (1.05 W cm$^2$ at 1073 K) with a low overpotential in the $H_2$ SOFC at 1073 K, which was approximately two-fold higher than that of the LSFM electrode (Ru > Ni > Fe ≥ Co). In the $CO_2$ electrolysis mode, the cell with the LSFM-Fe electrode achieved a current density of 2.201 A cm$^{-2}$ at 1123 K when a voltage of 1.5 V (Fe > Ru ≥ Co > Ni) was applied. Unlike the hydrogen application, the Fe catalyst exhibited better catalytic activity and accelerated the electrode surface exchange kinetics better than Ru in $CO_2$ reduction, and this was found from the polarization resistance obtained by using EIS, and the high-exchange current density. In addition, the distribution of the relaxation time results provides insights into the activity of each metal catalyst in the electrochemical $CO_2$ reduction. Consequently, the Fe and Ru catalysts exhibited a higher adsorption of $CO_2$ molecules, which is the starting step of the $CO_2$ reduction. The LSFM-Ni electrode showed a higher catalytic activity than the LSFM-Fe and LSFM-Ru electrodes because of the interaction of the catalyst with the carbonate intermediate and the LSFM structure. These results suggest that suitable metal catalysts should be explored from various perspectives, such as molecular adsorption and dissociation.

## Conflicts of interest

There are no conflicts to declare.

## Acknowledgements

## References

1 H. L. Van Soest, M. G. J. den Elzen and D. P. van Vuuren, Net-zero emission targets for major emitting countries consistent with the Paris Agreement, *Nat. Commun.*, 2021, **12**, 2140.

2 J. Rogelj, O. Geden, A. Cowie and A. Reisinger, Net-zero emissions targets are vague: three ways to fix, *Nature*, 2021, **591**, 365–368.

3 R. Meys, A. Kätelhön, M. Bachmann, B. Winter, C. Zibunas, S. Suh and A. Bardow, Achieving net-zero greenhouse gas emission plastics by a circular carbon economy, *Science*, 2021, **374**, 71–76.

4 H. J. Peng, M. T. Tang, J. H. Stenlid, X. Liu and F. Abild-Pedersen, Trends in oxygenate/hydrocarbon selectivity for electrochemical $CO_2$ reduction to $C_2$ products, *Nat. Commun.*, 2022, **13**, 1399.

5 E. H. Bennetzen, P. Smith and J. R. Porter, Decoupling of greenhouse gas emissions from global agricultural production: 1970-2050, *Glob. Chang. Biol.*, 2016, **22**, 763–781.

6 F. Ismail, A. Abdellah, H.-J. Lee, V. Sudheeshkumar, W. Alnoush and D. C. Higgins, Impact of nickel content on the structure and electrochemical $CO_2$ reduction performance of nickel-nitrogen-carbon catalysts derived from zeolitic imidazolate frameworks, *ACS Appl. Energy Mater.*, 2022, **5**, 430–439.

7 S. Nitopi, E. Bertheussen, S. B. Scott, X. Liu, A. K. Engstfeld, S. Horch, B. Seger, I. E. L. Stephens, K. Chan, C. Hahn, J. K. Nørskov, T. F. Jaramillo and I. Chorkendorff, Progress and perspectives of electrochemical $CO_2$ reduction on copper in aqueous electrolyte, *Chem. Rev.*, 2019, **119**, 7610–7672.

8 W. Ni, Z. Liu, Y. Zhang, C. Ma, H. Deng, S. Zhang and S. Wang, Electroreduction of carbon dioxide driven by the intrinsic defects in the carbon plane of a single Fe-N$_4$ site, *Adv. Mater.*, 2020, **33**, 2003238.

**3542** | *Inorg. Chem. Front.*, 2023, **10**, 3536–3543

This journal is © the Partner Organisations 2023

9 X. Su, X. F. Yang, Y. Huang, B. Liu and T. Zhang, Single-atom catalysis toward efficient $CO_2$ conversion to CO and formatde products, *Acc. Chem. Res.*, 2019, **52**, 656–664.

10 H. B. Yang, S.-F. Hung, S. Liu, K. Yuan, S. Miao, L. Zhang, X. Huang, H.-Y. Wang, W. Cai, R. Chen, J. Gao, X. Yang, W. Chen, Y. Huang, H. M. Chen, C. M. Li, T. Zhang and B. Liu, Atomically dispersed Ni(I) as the active site for electrochemical $CO_2$ reduction, *Nat. Energy*, 2018, **3**, 140–147.

11 W. Wang, S. Wang, X. Ma and J. Gong, Recent advances in catalytic hydrogenation of carbon dioxide, *Chem. Soc. Rev.*, 2011, **40**, 3703–3727.

12 X. Li, P. Anderson, H.-R. M. Jhong, M. Paster, J. F. Stubbins and P. J. A. Kenis, Greenhouse gas emissions, energy efficiency, and cost of synthetic fuel production using electrochemical $CO_2$ conversion and the Fischer–Tropsch process, *Energy Fuels*, 2016, **30**, 5980–5989.

13 R. Dictor, Fischer-Tropsch synthesis over reduced and unreduced iron oxide catalysts, *J. Catal.*, 1986, **97**, 121–136.

14 Z. Shao, S. M. Haile, J. Ahn, P. D. Ronney, Z. Zhan and S. A. Barnett, A thermally self-sustained micro solid-oxide fuel-cell stack with high power density, *Nature*, 2005, **435**, 795–798.

15 F. Bidrawn, G. Kim, G. CorreJ, T. S. Irvine, J. M. Vohs and R. J. Gorte, Efficient reduction of $CO_2$ in a solid oxide electrolyzer, *Electrochem. Solid-State Lett.*, 2008, **11**, B167.

16 E. P. Murray, T. Tsai and S. A. Barnett, A direct-methane fuel cell with a ceria-based anode, *Nature*, 1999, **400**, 649–651.

17 S. Lee, M. Kim, K. T. Lee, J. T. S. Irvine and T. H. Shin, Enhancing electrochemical $CO_2$ reduction using $Ce(Mn,Fe)O_2$ with $La(Sr)Cr(Mn)O_3$ cathode for high–temperature solid oxide electrolysis cells, *Adv. Energy Mater.*, 2021, **11**, 2100339.

18 Y. Song, X. Zhang, K. Xie, G. Wang and X. Bao, High–temperature $CO_2$ electrolysis in solid oxide electrolysis cells: developments, challenges, and prospects, *Adv. Mater.*, 2019, **31**, e1902033.

19 C. Sun, R. Hui and J. Roller, Cathode materials for solid oxide fuel cells: a review, *J. Solid State Electrochem.*, 2010, **14**, 1125–1144.

20 R. Ren, Z. Wang, X. Meng, C. Xu, J. Qiao, W. Sun and K. Sun, Boosting the electrochemical performance of Fe-based layered double perovskite cathodes by $Zn^{2+}$ doping for solid oxide fuel cells, *ACS Appl. Mater. Interfaces*, 2020, **12**, 23959–23967.

21 E. A. Kotomin, Y. A. Mastrikov, M. M. Kuklja, R. Merkle, A. Roytburd and J. Maier, First principles calculations of oxygen vacancy formation and migration in mixed conducting $Ba_{0.5}Sr_{0.5}Co_{1-y}Fe_yO_{3-\delta}$ perovskites, *Solid State Ionics*, 2011, **188**, 1–5.

22 T. Ishihara, K.-T. Wu and S. Wang, High temperature $CO_2$ electrolysis on $La(Sr)Fe(Mn)O_3$ oxide cathode by using $LaGaO_3$ based electrolyte, *ECS Trans.*, 2015, **66**, 197–205.

23 X. Peng, Y. Tian, Y. Liu, W. Wang, L. Jia, J. Pu, B. Chi and J. Li, An efficient symmetrical solid oxide electrolysis cell with LSFM-based electrodes for direct electrolysis of pure $CO_2$, *J. CO$_2$ Util.*, 2020, **36**, 18–24.

24 S. Wang, H. Tsuruta, M. Asanuma and T. Ishihara, Ni-Fe-La $(Sr)Fe(Mn)O_3$ as a new active cermet cathode for intermediate-temperature $CO_2$ electrolysis using a $LaGaO_3$-based electrolyte, *Adv. Energy Mater*, 2014, **5**, 1401003.

25 Y. Zhou, L. Lin, Y. Song, X. Zhang, H. Lv, Q. Liu, Z. Zhou, N. Ta, G. Wang and X. Bao, Pd single site-anchored perovskite cathode for $CO_2$ electrolysis in solid oxide electrolysis cells, *Nano Energy*, 2020, **71**, 104598.

26 W. Wang, L. Gan, J. P. Lemmon, F. Chen, J. T. S. Irvine and K. Xie, Enhanced carbon dioxide electrolysis at redox manipulated interfaces, *Nat. Commun.*, 2019, **10**, 1550.

27 J. T. S. Irvine, D. Neagu, M. C. Verbraeken, C. Chatzichristodoulou, C. Graves and M. B. Mogensen, Evolution of the electrochemical interface in high-temperature fuel cells and electrolysers, *Nat. Energy*, 2016, **1**, 1–13.

28 J. Hong, A. Bhardwaj, Y. Namgung, H. Bae and S. Song, Evaluation of the effects of nanocatalyst infiltration on the SOFC performance and electrode reaction kinetics using the transmission line model, *J. Mater. Chem. A*, 2020, **8**, 23473–23487.

29 G. Chiodelli and L. Malavasi, Electrochemical open circuit voltage (OCV) characterization of SOFC materials, *Ionics*, 2013, **19**, 1135–1144.

30 Z. Fan and F. B. Prinz, Enhancing oxide ion incorporation kinetics by nanoscale yttria-doped ceria interlayers, *Nano Lett.*, 2011, **11**, 2202–2205.

31 S. Lee, S. H. Woo, T. H. Shin and J. T. S. Irvine, Pd and GDC Co-infiltrated LSCM cathode for high-temperature $CO_2$ electrolysis using solid oxide electrolysis cells, *Chem. Eng. J.*, 2021, **420**, 127706.

32 R. O'Hayre, S. W. Cha, W. Colella and F. B. Prinz, *Fuel Cell Fundamentals*, *John Wiley & Sons, Inc.*, 2016.

33 P. Caliandro, A. Nakajo, S. Diethelm and J. V. Van Herle, Model-assisted identification of solid oxide cell elementary processes by electrochemical impedance spectroscopy measurements, *J. Power Sources*, 2019, **436**, 226838.

34 K. Huang, R. Tichy, J. B. Goodenough and C. Milliken, Superior perovskite oxide–ion conductor; strontium– and magnesium–doped $LaGaO_3$: III, Performance tests of single ceramic fuel cells, *J. Am. Ceram. Soc.*, 1998, **81**, 2581–2585.

35 Y. Li, B. Hu, C. Xia, W. Q. Xu, J. P. Lemmon and F. Chen, A novel fuel electrode enabling direct $CO_2$ electrolysis with excellent and stable cell performance, *J. Mater. Chem. A*, 2017, **5**, 20833–20842.

36 X. Yang, W. Sun, M. Ma, C. Xu, R. Ren, J. Qiao, Z. Wang, Z. Li, S. Zhen and K. Sun, Achieving highly efficient carbon dioxide electrolysis by in situ construction of the heterostructure, *ACS Appl. Mater. Interfaces*, 2021, **13**, 20060–20069.

This journal is © the Partner Organisations 2023

*Inorg. Chem. Front.*, 2023, **10**, 3536–3543 | **3543**